Hybrid Two-Fluid DEM Simulation of Gas-Solid Fluidized Beds

Jin Sun[1]
e-mail: jinsun@iastate.edu

Francine Battaglia

Shankar Subramaniam

Department of Mechanical Engineering,
Iowa State University,
Ames, IA 50011

Simulations of gas-solid fluidized beds have been performed using a hybrid simulation method, which couples the discrete element method (DEM) for particle dynamics with the averaged two-fluid (TF) continuum equations for the gas phase. The coupling between the two phases is modeled using an interphase momentum transfer term. The results of the hybrid TF-DEM simulations are compared to experimental data and TF model simulations. It is found that the TF-DEM simulation is capable of predicting general fluidized bed dynamics, i.e., pressure drop across the bed and bed expansion, which are in agreement with experimental measurements and TF model predictions. Multiparticle contacts and large contact forces distribute in the regions away from bubbles, as demonstrated from the TF-DEM simulation results. The TF-DEM model demonstrates the capability to capture more heterogeneous structural information of the fluidized beds than the TF model alone. The implications to the solid phase constitutive closures for TF models are discussed. However, the TF-DEM simulations depend on the form of the interphase momentum transfer model, which can be computed in terms of averaged or instantaneous particle quantities. Various forms of the interphase momentum transfer model are examined, and simulation results from these models are compared. [DOI: 10.1115/1.2786530]

Keywords: fluidized bed, discrete element method, two-fluid model

Introduction

Gas-solid fluidized beds are widely used in many industrial applications, e.g., fluid catalytic cracking, due to the contact between gas and solid phases, which prompts rapid heat and mass transfer and fast chemical reactions. However, the dynamics of gas-solid fluidized beds need to be better understood in order to improve existing processes and scale up new processes. Reliable simulation tools can provide valuable insights into gas-solid flow processes and, as a result, accelerate the achievement of substantial process improvements [1].

The dynamics of fluidized beds can be described at different levels of detail [2]. At the most fundamental level (atomic or molecular scale is not considered), the motion of the whole system is determined by the Newtonian equations of motion for the translation and rotation of each particle, and the Navier–Stokes and continuity equations. The fluid motion and particle motion are linked by the no-slip condition on each particle boundary. At the second level, the fluid velocity at each point is replaced by its average, taken over a spatial domain large enough to contain many particles but still small compared to the whole region occupied by the flowing mixture. The Newtonian equations of motion are solved for each particle in a Lagrangian framework. The coupling force between fluid and particles is then related to the particle's velocity relative to the locally averaged fluid velocity and to the local concentration of the particle assembly. At a third level, both the fluid velocity and the particle velocity are averaged over local spatial domains. A description at this level of detail is often referred as the two-fluid model (TFM).

The kinetic theory of granular flows (KTGF) has been successfully applied to the TFM for fluidization in the last decade [3]. The KTGF has a basic assumption that particle collisions are instantaneous and binary. However, questions about the validity and capability of KTGF arise because of the microstructures formed in the fluidized beds, e.g., clusters in a riser [4] and "defluidized" zones in a bubbling fluidized bed [5]. In a dense bubbling fluidized bed, the particle pressure around a bubble was experimentally measured and shown to be large in the region far below the bubble where there is no agitation [5]. These facts lead to speculations that lasting multiple contacts in dense fluidized beds limit the application of KTGF. Previous experiments [6] and models [7,8] also showed that diffusion and mixing are dominated by geometry, consistent with long-lasting contacts (but not thermal collisions) in dense granular flows. However, there has not yet been a quantitative analysis to assess multiparticle microstructures under certain fluidization conditions or how the microstructures affect the constitutive behavior of a dense fluidized bed. A good understanding of the spatial distribution and temporal evolution of multiparticle contacts and corresponding particle contact forces is a necessary step toward developing constitutive models that can accurately predict fluidized bed dynamics.

In this paper, a hybrid model at the second level will be employed to improve the understanding of multiparticle contacts in a fluidized bed. The hybrid model couples a TFM to solve the gas phase with the discrete element method (DEM) to solve the particle motion equations. Therefore, the hybrid model can simulate a fluidized bed at particle scales and produce useful information to analyze the microstructures as well as particle dynamics. The computational results from the hybrid model will be compared and validated with experimental and TFM results. A key consideration in the hybrid model is the coupling between the phases, i.e., the fluid-particle interaction force. Different formulations have been used to calculate and transfer the force between phases [9–12]. However, formulations have not been thoroughly analyzed for different flow conditions. In this paper, two different ways to transfer the effective drag force, an important coupling term between gas and particles, will be discussed, and simulation results from these two methods will be compared.

Methodology

Multifluid Model. The multifluid Eulerian model describes the gas phase and solid phases as interpenetrating continua. The particle mixture is divided into a discrete number of phases, each of which can have different physical properties, e.g., particle diam-

[1]Corresponding author.

Contributed by the Fluids Engineering Division of ASME for publication in the JOURNAL OF FLUIDS ENGINEERING. Manuscript received August 28, 2006; final manuscript received June 9, 2007. Review conducted by Ye Zhou. Paper presented at the 2006 ASME International Mechanical Engineering Congress (IMECE2006), Chicago, IL, November 5–10, 2006.

eter. It should be noted that the TFM for a gas phase and single solid phase is a special case, $m=1$, for the general formula presented next. The governing equations for the multifluid model are [13]

Continuity equation for the gas phase:

$$\frac{\partial}{\partial t}(\varepsilon_g \rho_g) + \nabla \cdot (\varepsilon_g \rho_g \mathbf{v}_g) = \sum_{n=1}^{N_g} R_{gn} \tag{1}$$

Continuity equation for the mth solid phase:

$$\frac{\partial}{\partial t}(\varepsilon_{sm} \rho_{sm}) + \nabla \cdot (\varepsilon_{sm} \rho_{sm} \mathbf{v}_{sm}) = \sum_{n=1}^{N_{sm}} R_{smn} \tag{2}$$

Momentum equation for the gas phase:

$$\frac{\partial}{\partial t}(\varepsilon_g \rho_g \mathbf{v}_g) + \nabla \cdot (\varepsilon_g \rho_g \mathbf{v}_g \mathbf{v}_g) = \nabla \cdot \bar{\bar{S}}_g + \varepsilon_g \rho_g \mathbf{g} - \sum_{m=1}^{M} \mathbf{I}_{gm} \tag{3}$$

Momentum equation for the mth solid phase:

$$\frac{\partial}{\partial t}(\varepsilon_{sm} \rho_{sm} \mathbf{v}_{sm}) + \nabla \cdot (\varepsilon_{sm} \rho_{sm} \mathbf{v}_{sm} \mathbf{v}_{sm}) = \nabla \cdot \bar{\bar{S}}_{sm} + \varepsilon_{sm} \rho_{sm} \mathbf{g} + \mathbf{I}_{gm} - \sum_{\substack{l=1 \\ l \neq m}}^{M} \mathbf{I}_{ml} \tag{4}$$

Translational granular temperature equation [4]:

$$\frac{3}{2}\left[\frac{\partial}{\partial t}(\varepsilon_{sm} \rho_{sm} \theta_{sm,t}) + \nabla \cdot (\varepsilon_{sm} \rho_{sm} \theta_{sm,t} \mathbf{v}_{sm})\right] = -\nabla \cdot \mathbf{q}_{sm} - \bar{\bar{S}}_{sm} : \nabla \mathbf{v}_{sm} + \gamma_{sm,\text{slip}} - J_{sm,\text{coll}} - J_{sm,\text{vis}} \tag{5}$$

where the translational granular temperature is defined as

$$\theta_{sm,t} = \frac{1}{3}\langle C_{pi}^2 \rangle \tag{6}$$

The fluctuation in the particle translational velocity shown in Eq. (6) is defined as $\mathbf{C}_{pi}=\mathbf{v}_{pi}-\mathbf{v}_{sm}$, where $\mathbf{v}_{pi}$ is the instantaneous translational particle velocity and the symbol $\langle\ \rangle$ designates the operation of taking average.

The constitutive equations for the solid phases were derived for granular flows [14]. There are two distinct flow regimes in granular flows: a viscous or rapidly shearing regime in which stresses arise due to collisional or translational momentum transfer and a plastic or slowly shearing regime in which stresses arise due to Coulomb friction between grains in close contact. Two different approaches are used for these regimes:

$$\bar{\bar{S}}_{sm} = \begin{cases} -P_{sm}^{p}\bar{\bar{I}} + \bar{\bar{\tau}}_{sm}^{p} & \text{if } \varepsilon_s \geqslant \varepsilon_s^* \\ -P_{sm}^{v}\bar{\bar{I}} + \bar{\bar{\tau}}_{sm}^{v} & \text{if } \varepsilon_s < \varepsilon_s^* \end{cases} \tag{7}$$

where P_{sm}^{p} and $\bar{\bar{\tau}}_{sm}^{p}$ are the pressure and the viscous stress in the mth solid phase for the plastic regime, P_{sm}^{v} and $\bar{\bar{\tau}}_{sm}^{v}$ are the pressure and the viscous stress for the viscous regime, and ε_g^* is a critical packing solid volume fraction, set to 0.58 for the simulations in this paper.

The granular stress equation based on KTGF [15] is applied to the viscous regime. The granular pressure and stresses are given by

$$P_{sm}^{v} = K_{1m}\varepsilon_{sm}^2 \theta_{sm,t} \tag{8}$$

$$\bar{\bar{\tau}}_{sm}^{v} = 2\mu_{sm}^{v}\bar{\bar{D}}_{sm} + \lambda_{sm}^{v}\,\text{tr}(\bar{\bar{D}}_{sm})\bar{\bar{I}} \tag{9}$$

where λ_{sm}^{v} is the second coefficient of viscosity,

$$\lambda_{sm}^{v} = K_{2m}\varepsilon_{sm}\sqrt{\theta_{sm,t}} \tag{10}$$

The shear viscosity factor μ_{sm}^{v} is

$$\mu_{sm}^{v} = K_{3m}\varepsilon_{sm}\sqrt{\theta_{sm,t}} \tag{11}$$

The strain rate tensor $\bar{\bar{D}}_{sm}$ is given by

$$\bar{\bar{D}}_{sm} = \frac{1}{2}[\nabla \mathbf{v}_{sm} + (\nabla \mathbf{v}_{sm})^T] \tag{12}$$

The coefficients K_{1m}, K_{2m}, and K_{3m} are functions of particle density, diameter, restitution coefficient, radial distribution function, and local volume fractions. The solid stress tensor in the viscous regime only takes into account contributions from particle translational momentum flux and binary collisions. In the plastic flow regime, the solid stress tensor was derived based on plastic flow theory [16] and critical state theory [17].

The constitutive equation for the gas phase stress tensor is

$$\bar{\bar{S}}_g = -P_g\bar{\bar{I}} + \bar{\bar{\tau}}_g \tag{13}$$

where P_g is the gas pressure and $\bar{\bar{I}}$ is the identity tensor. The viscous stress tensor $\bar{\bar{\tau}}_g$ is assumed to be of the Newtonian form

$$\bar{\bar{\tau}}_g = 2\mu_g\bar{\bar{D}}_g + \lambda_g \nabla \cdot \mathbf{v}_g \tag{14}$$

where $\bar{\bar{D}}_g$ is the strain rate tensor for the gas phase. The gas-solid momentum transfer ($\mathbf{I}_{gm}$) will be discussed in the subsection on coupling TFM and DEM.

Discrete Element Method. Individual particle motion in a fluidized bed can be described by Newtonian equations of motion, which is a Lagrangian approach. The DEM employs numerical integration of the equations of motion to resolve particle trajectories [18]. The translational and rotational motions of a particle are governed by

$$m_i\frac{d\mathbf{v}_{pi}}{dt} = \mathbf{f}_{ci} + \mathbf{f}_{gpi} + m_i\mathbf{g} \tag{15}$$

$$I_i\frac{d\boldsymbol{\omega}_i}{dt} = \mathbf{T}_i \tag{16}$$

where $\mathbf{f}_{ci}$ is the particle-particle contact force, $\mathbf{f}_{gpi}$ is the fluid-particle interaction force, $m_i\mathbf{g}$ is the gravitational force, $\mathbf{T}_i$ is the torque arising from the tangential components of the contact force, and I_i, $\mathbf{v}_{pi}$, and $\boldsymbol{\omega}_i$ are the moment of inertia, linear velocity, and angular velocity, respectively. The net contact force $\mathbf{f}_{ci}$ and torque $\mathbf{T}_i$ acting on each particle result from a vector summation of the force and torque at each particle-particle contact. A linear spring-dashpot model is employed for the contact force model due to its simplicity and reasonable accuracy [18]. The basic principles of the linear spring-dashpot model are briefly described in the following.

Two contacting particles $\{i,j\}$ are shown in Fig. 1 with radii $\{a_i,a_j\}$ at positions $\{\mathbf{r}_i,\mathbf{r}_j\}$, with velocities $\{\mathbf{v}_i,\mathbf{v}_j\}$ and angular velocities $\{\boldsymbol{\omega}_i,\boldsymbol{\omega}_j\}$. The normal compression δ_{ij}, relative normal velocity $\mathbf{v}_{n_{ij}}$, and relative tangential velocity $\mathbf{v}_{t_{ij}}$ are [19]

$$\delta_{ij} = d - r_{ij} \tag{17}$$

$$\mathbf{v}_{n_{ij}} = (\mathbf{v}_{ij} \cdot \mathbf{n}_{ij})\mathbf{n}_{ij} \tag{18}$$

$$\mathbf{v}_{t_{ij}} = \mathbf{v}_{ij} - \mathbf{v}_{n_{ij}} - (a_i\boldsymbol{\omega}_i + a_j\boldsymbol{\omega}_j) \times \mathbf{n}_{ij} \tag{19}$$

where $d=a_i+a_j$, $\mathbf{r}_{ij}=\mathbf{r}_i-\mathbf{r}_j$, and $\mathbf{n}_{ij}=\mathbf{r}_{ij}/r_{ij}$, with $r_{ij}=|\mathbf{r}_{ij}|$ and $\mathbf{v}_{ij}=\mathbf{v}_i-\mathbf{v}_j$. The rate of change of the elastic tangential displacement $\mathbf{u}_{t_{ij}}$, set to zero at the initiation of a contact, is

$$\frac{d\mathbf{u}_{t_{ij}}}{dt} = \mathbf{v}_{t_{ij}} - \frac{(\mathbf{u}_{t_{ij}} \cdot \mathbf{v}_{ij})\mathbf{r}_{ij}}{r_{ij}^2} \tag{20}$$

The last term in Eq. (20) arises from the rigid body rotation around the contact point and ensures that $\mathbf{u}_{t_{ij}}$ always lies in the

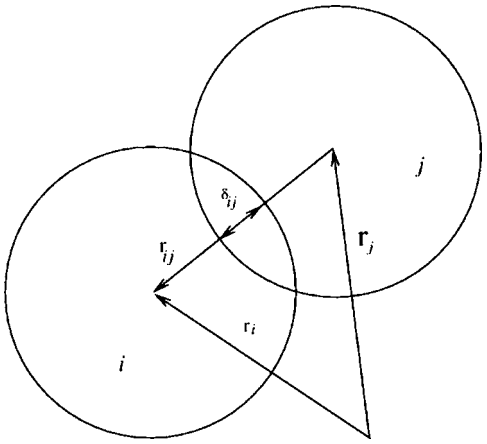

Fig. 1 Schematic of two particles *i* and *j* in contact and position vectors $\mathbf{r}_i$ and $\mathbf{r}_j$, respectively, with overlap δ_{ij}

local tangent plane of contact. Normal and tangential forces acting on particle i are

$$\mathbf{F}_{n_{ij}} = f(\delta_{ij}/d)(k_n \delta_{ij} \mathbf{n}_{ij} - \gamma_n m_{\text{eff}} \mathbf{v}_{n_{ij}}) \tag{21}$$

$$\mathbf{F}_{t_{ij}} = f(\delta_{ij}/d)(-k_t \mathbf{u}_{t_{ij}} - \gamma_t m_{\text{eff}} \mathbf{v}_{t_{ij}}) \tag{22}$$

where $k_{n,t}$ and $\gamma_{n,t}$ are the spring stiffness and viscoelastic constants, respectively, and $m_{\text{eff}}=m_i m_j/(m_i+m_j)$ is the effective mass of the spheres with masses m_i and m_j. The corresponding contact force on particle j is simply given by Newton's third law, i.e., $\mathbf{F}_{ji}=-\mathbf{F}_{ij}$. The function $f(\delta_{ij}/d)=1$ is for the linear spring-dashpot model, and $f(\delta_{ij}/d)=\sqrt{\delta_{ij}/d}$ is for Hertzian contacts with viscoelastic damping between spheres.

Static friction is implemented by keeping track of the elastic shear displacement throughout the lifetime of a contact. The static yield criterion, characterized by a local particle friction coefficient μ, is modeled by truncating the magnitude of $\mathbf{u}_{t_{ij}}$ as necessary to satisfy $|\mathbf{F}_{t_{ij}}| < |\mu \mathbf{F}_{n_{ij}}|$. Thus, the contact surfaces are treated as "sticking" when $|\mathbf{F}_{t_{ij}}| < |\mu \mathbf{F}_{n_{ij}}|$ and as "slipping" when the yield criterion is satisfied. The total contact force and torque acting on particle i are then given by

$$\mathbf{f}_{ci} = \sum_j (\mathbf{F}_{nij} + \mathbf{F}_{tij}) \tag{23}$$

$$\mathbf{T}_i = -\frac{1}{2} \sum_j \mathbf{r}_{ij} \times \mathbf{F}_{tij} \tag{24}$$

The amount of energy lost in collisions, characterized by the inelasticity through the value of the coefficient of restitution e, is defined as the negative ratio of the particle velocity after collision to the velocity before collision. For the linear spring-dashpot model, the coefficient of normal restitution e_n and contact time t_c can be analytically obtained,

$$e_n = \exp(-\gamma_n t_c/2) \tag{25}$$

where the contact time t_c is given by

$$t_c = \pi (k_n/m_{\text{eff}} - \gamma_n^2/4)^{-1/2} \tag{26}$$

The value of the spring constant should be large enough to avoid particle interpenetration, yet not so large as to require an unreasonably small simulation time step δt since an accurate simulation typically requires $\delta t \sim t_c/50$. After the contact force is calculated, the equations of motion, which are ordinary differential equations, can be numerically integrated to get the particle trajectories.

Coupling of the Two-Fluid Model and Discrete Element Method. A hybrid model at the second level is constructed by coupling the TFM for the gas phase with DEM for the particle motion [20]. The coupling term between the equations for gas and particle motion is the gas-particle interaction $\mathbf{I}_{gm}$ in the gas momentum equation and $\mathbf{f}_{gpi}$ in the particle equation of motion. Due to the averaging process in the derivation of momentum equations for the TFM, the fluid-particle interaction force may be written as the sum of a component due to macroscopic variations in the fluid stress tensor and a component representing the effect of variations in the point stress stress tensor as the gas flows around the particle [21]. For the gas force on a particle,

$$\mathbf{f}_{gpi} = V_{pi} \nabla \cdot \bar{\bar{S}}_g + \mathbf{f}'_{gpi} \tag{27}$$

where V_{pi} is the volume of particle i. The first term on the right in Eq. (27) accounts for the macroscopic variation in the fluid stress tensor. The second term on the right in Eq. (27) includes skin friction and drag contributions accounting for the detailed variation in the stress tensor. In general, the term comprises an effective drag force in the direction of the relative velocity between the fluid and particle, and a virtual or added mass force accounting for the resistance of the fluid mass that is moving at the same acceleration as the particle. For gas-solid flows, the virtual mass force may be neglected and $\mathbf{f}'_{gpi}$ reduces to an effective drag force, which should be the product of the local void fraction ε_g and the drag force $\mathbf{f}_{di}$ obtained from experimentally based correlations. Substituting Eq. (13) to Eq. (27),

$$\mathbf{f}_{gpi} = -V_{pi} \nabla P_g + V_{pi} \nabla \cdot \bar{\bar{\tau}}_g + \varepsilon_g \mathbf{f}_{di} \tag{28}$$

The drag force on a single particle of diameter d_{pi} in a multiparticle system can be calculated from the correlation,

$$\mathbf{f}_{di} = \frac{1}{2} C_{Di} \rho_g \frac{\pi d_{pi}^2}{4} \varepsilon_g^2 |\mathbf{v}_g^i - \mathbf{v}_{pi}| (\mathbf{v}_g^i - \mathbf{v}_{pi}) f(\varepsilon_g) = \frac{\pi d_{pi}^3}{6 \varepsilon_g \varepsilon_{sm}} \beta (\mathbf{v}_g^i - \mathbf{v}_{pi}) \tag{29}$$

where $\mathbf{v}_g^i$ is the gas velocity at the location of particle i and $f(\varepsilon_g)$ is a function of the local void fraction. The single particle velocity $\mathbf{v}_{pi}$ is used since the correlations relate the effective drag force to that of a single particle in the absence of other particles. The expressions of β are extended from the work of Ergun [22] and Wen and Yu [23], and were used by Tsuji et al. [9],

$$\beta = \begin{cases} 150 \dfrac{\varepsilon_{sm}^2}{\varepsilon_g d_{pi}^2} \mu_g + 1.75 \varepsilon_{sm} \dfrac{\rho_g}{d_{pi}} |\mathbf{v}_g^i - \mathbf{v}_{pi}| & \text{for } \varepsilon_g \leqslant 0.8 \\ \dfrac{3}{4} C_D \dfrac{\varepsilon_g \varepsilon_{sm}}{d_{pi}} \rho_g |\mathbf{v}_g^i - \mathbf{v}_{pi}| \varepsilon_g^{-2.7} & \text{for } \varepsilon_g > 0.8 \end{cases} \tag{30}$$

The drag coefficient C_{Di} depends on the particle Reynolds number $\text{Re}_{pi}=(d_{pi}\varepsilon_g|\mathbf{v}_g^i-\mathbf{v}_{pi}|\rho_g)/\mu_g$, and is given by

$$C_{Di} = \begin{cases} 24(1 + 0.15 \text{Re}_{pi}^{0.687})/\text{Re}_{pi} & \text{for } \text{Re}_{pi} < 1000 \\ 0.43 & \text{for } \text{Re}_{pi} \geqslant 1000 \end{cases} \tag{31}$$

The fluid-particle interaction force per unit volume of bed, $\mathbf{I}_{gm}$, in the gas momentum equation (refer to Eq. (3)) is obtained by summing the gas forces $\mathbf{f}_{gpi}$ over all the particles in a fluid cell and dividing by the volume of the fluid cell, V_{cell}. Thus,

$$\mathbf{I}_{gm} = \frac{\sum_i^{N_m} \mathbf{f}_{gpi}}{V_{\text{cell}}} = -\varepsilon_{sm} \nabla P_g + \varepsilon_{sm} \nabla \cdot \bar{\bar{\tau}}_g + \sum_i^{N_m} \varepsilon_g \mathbf{f}_{di}/V_{\text{cell}} \tag{32}$$

where N_m is the number of particles of the mth phase in a fluid cell. The last term in Eq. (32) may be calculated approximately using local mean gas and particle velocities,

$$\sum_{i}^{N_m} \varepsilon_g \mathbf{f}_{di} / V_{\text{cell}} = \beta(\mathbf{v}_g - \mathbf{v}_{sm}) \tag{33}$$

where β uses the same form as in Eq. (30), except that the velocity $\mathbf{v}_{pi}$ is replaced by the local mean value in a fluid cell, i.e., $\mathbf{v}_{sm}$.

The solid volume fraction and local mean solid velocities are evaluated in a fluid computational cell,

$$\varepsilon_{sm} = \frac{\sum_{i}^{N_m} V_{pi}}{V_{\text{cell}}} \tag{34}$$

$$\mathbf{v}_{sm} = \frac{\sum_{i}^{N_m} \mathbf{v}_{pi} V_{pi}}{\sum_{i}^{N_m} V_{pi}} \tag{35}$$

The volume of a computational cell, V_{cell}, in two-dimensional (2D) simulations is calculated using the diameter of a spherical particle as the cell thickness in the third dimension.

Based on the previous discussion, it can be seen that the fluid-particle effective drag force can be calculated in two ways to transfer the effects between gas and particle motions. The first method is to calculate the drag force using Eq. (33) in a fluid cell and then assign this mean drag force back to each particle in the cell. This method, with the assumption that particles in a cell with the same diameter have the same drag force, is used for most of the simulations in this paper. The second method is to calculate the drag force on each particle using Eq. (29) and then sum up the particle drag forces in a fluid cell as the total drag force on the fluid according to Newton's third law. This method is employed for one case as a comparison to the results from the first method. However, it should be noted that further assumptions are made in this paper. One assumption is that the total drag force on the gas is calculated using Eq. (33) and is approximately equal in magnitude to that obtained from the summation of each particle's drag force. For the second method, Eq. (33) is also used for calculating the drag force on the gas phase, and the only difference between these methods is the way to obtain the drag force on the particles. Finally, the viscous stress gradient in Eq. (28) is neglected.

Numerical Formulation. A FORTRAN code, multiphase flow with interphase exchanges (MFIX), is used for all simulations in this work. MFIX uses a finite volume approach with a staggered grid for the discretization of the TFM governing equations to reduce numerical instabilities [24]. Scalars such as pressure and volume fraction are stored at the cell centers, and the velocity components are stored at cell surfaces. A second-order discretization is used for spatial derivatives and first-order discretization for temporal derivatives. A modified SIMPLE algorithm is employed to solve the discretized equations [24]. The explicit time integration method is used to solve the translational and rotational motion equations used in the DEM [10,18].

Simulation Conditions

Gas-solid fluidized beds were simulated using the hybrid TFM-DEM model presented in the methodology subsection (for $m=1$). The fluidized beds have very small depths compared to the other two dimensions. Therefore, 2D simulations were performed, which also reduces the computational requirements needed for three dimensional (3D) simulations. The first computational case simulates a fluidized bed experiment with a central air jet flow, presented by Tsuji et al. [9]. This case will be referred to as the central-jet case, hereafter. The computational domain is shown in Fig. 2(*a*), and the simulation parameters are listed in Table 1. Most particle parameters are set to be the same as what were used in the experiment. One important difference between the computational setup and the experimental setup is that there is only one layer of particles in the thin depth direction for computations, while there were about five particle layers in the experiment. A second simulation for a bubbling fluidized bed with a uniform inflow was performed to analyze a different flow situation, where the bed is fluidized by a uniform air inflow. The simulations were based on the experiment of the bubbling fluidized bed by Goldschmidt et al. [25]. This case will be referred to as the uniform

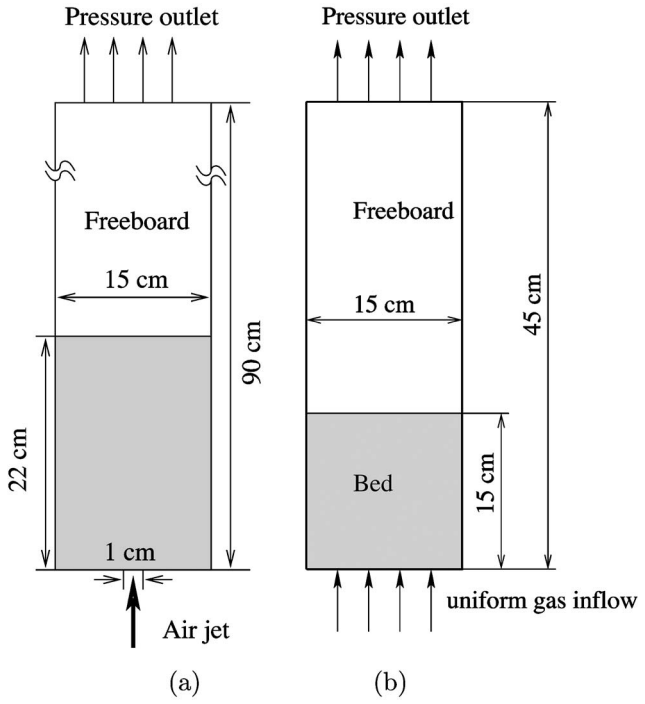

Fig. 2 Schematic showing computational domains for the experiments of (*a*) Tsuji et al. [9] and (*b*) Goldschmidt et al. [25]

Table 1 Computational parameters and general initial and boundary conditions for the experiments of Tsuji et al. [9] and Goldschmidt et al. [25]

	Ref. [9]	Ref. [25]
Geometry		
Height of domain (cm)	90	45
Width of domain (cm)	15	15
Horizontal grid size, Δx (cm)	1	1
Vertical grid size, Δy (cm)	2	1
Particle properties		
Particle diameter (cm)	0.4	0.25
Particle density (g/cm^3)	2.7	2.526
Particle stiffness coefficient (dyn/cm)	8×10^5	8×10^5
Particle damping coefficient (dyn s/cm)	18	1.77
Particle friction coefficient	0.2	0.1
Particle number	2400	4000
Initial conditions		
ε_g	1.0	1.0
$v_g(=U_{\text{mf}})$ (cm/s)	180	128
Initial bed height (cm)	22	15
Boundary conditions		
Central air jet inflow (cm/s)	3900	$1.5U_{\text{mf}}$
Specified pressure at outlet (Pa)	101325	101325
Wall boundary for gas phase	No slip	No slip
Wall stiffness coefficient (dyn/cm)	1.2×10^6	1.2×10^6
Wall damping coefficient (dyn s/cm)	22	3.93

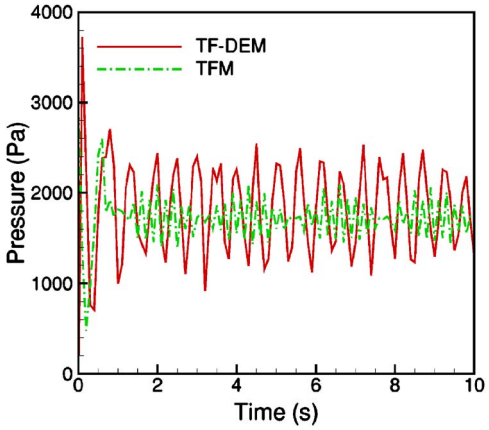

Fig. 3 Pressure drop at 20 cm above the inlet boundary fluctuates with time for the central-jet fluidized bed

inflow case, hereafter. The simulation was set up using the same conditions as in the experiment, except that there is only one layer of particles in the third dimension. The computational domain is shown in Fig. 2(*b*), and parameters are shown in Table 1.

The particle response to the flow fields in these simulations can be analyzed as follows to further elucidate and justify the hybrid method used. The particle Stokes number is defined as

$$\mathrm{St} = \frac{\tau_p}{\tau_g} \tag{36}$$

where $\tau_p = \rho_p d^2/18\mu$ is the particle Stokesian relaxation time and $\tau_g = d/\mathbf{v}_g$ can be deemed as a characteristic time scale for gas momentum convection over one particle diameter. Taking the uniform inflow case as an example, the Stokes number $\mathrm{St} \approx 37{,}422$ and the particle volume fractions are typically greater than 0.1 in the bed. In such a dense particle flow with very high Stokes number, gas turbulence is damped and small scale gas velocity fluctuations do not affect the particle dynamics significantly. Therefore, directly modeling the subgrid gas velocities is not considered in this paper.

Simulations using the TFM for both cases were also carried out using the same grid resolutions corresponding to those listed in Table 1. However, the particle motion is modeled by the solid phase equations in the TFM instead of using DEM directly. All the cases were simulated for 20 s of simulation time. The computational times used by the TFM and the hybrid method for the central-jet case were 5350 s and 6780 s, respectively, on one Opteron 270 (2.0 GHz) processor. Only results for the first 10 s will be presented in the next section since it was found that the fluidized beds reached a quasisteady state after approximately 5 s.

Results and Discussion

Computational results obtained from the simulation of the central-jet case are first presented. The pressure drop at 20 cm above the inlet boundary obtained from the TF-DEM simulation, as shown in Fig. 3, is similar to the computational findings of Tsuji et al.; i.e., the frequency and magnitude of fluctuation are in good agreement with experiments but with a higher mean pressure [9]. The TFM predicts that the pressure drop fluctuates around a similar mean pressure, but with a smaller fluctuating amplitude. This is probably because averaged equations are solved in the TFM. A refined grid with $\Delta x = 1$ cm and $\Delta y = 1$ cm is used to determine the grid dependence of this hybrid method. Statistical error in the particle field estimation becomes larger as the grid is refined due to the grid-cell-based averaging technique used in this paper. The comparison between the temporally averaged solid volume fraction distributions calculated from the coarse and fine grids is shown in Fig. 4. It can be seen that the result from the fine

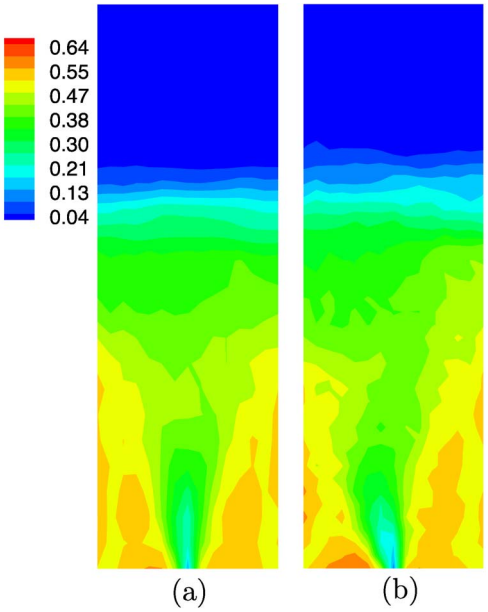

Fig. 4 The averaged (5–10 s) particle volume fractions for the central-jet fluidized bed for (*a*) the coarse grid with $\Delta x = 1$ cm and $\Delta y = 2$ cm and (*b*) the fine grid with $\Delta x = 1$ cm and $\Delta y = 1$ cm. The domain in the figure only shows 45 cm above the inlet.

grid shows a slightly higher bed expansion and a more asymmetric solid distribution with respect to the central jet. A method to address the particle field estimation problem will be discussed in the conclusions. The difference caused by the grid refinement, however, does not alter the comparison between the hybrid method and TFM made in this paper. The coarse grid was also used in previous computational studies [9,11]. The coarse grid results are thus shown in the following. The choice of the grid for the uniform inflow case is based on our grid refinement study for the TFM simulations of the same systems [26]. The logic is that this grid should capture enough details of the gas field and particle field as shown in the TFM simulations. It has been shown that the grid of cell size $\Delta x = 1$ cm and $\Delta y = 1$ cm produced an average error of 1.4% and a maximum error of 3.7% in time-averaged volume fraction, compared to the Richardson extrapolation results, and that further grid refinement had little influence on the results [26].

The bulk coordination number is defined as the average number of contacting neighbors of a particle. The time evolution of bulk coordination number can be used to characterize dynamic responses of granular systems [27]. The bulk coordination number corresponds to the first peak in the isotropic radial distribution function $g(r)$ and is a measure of order in the particle pattern. Thus, it can indirectly give a sense of whether the particle phase is more "gaslike" or "liquidlike." The isotropic radial distribution function $g(r)$ cannot be rigorously defined in the anisotropic configurations used in the simulations and is not presented in the paper. The bulk coordination numbers varying with time for the two simulations are shown in Fig. 5. The bulk coordination number for the central-jet case varies around 1.2, which indicates pair structures or other multicontact structures that exist in the system. In contrast, the bulk coordination number for the uniform inflow case varies around 0.5, which indicates that structures with contacting particles do not prevail. To further elucidate the spatial variation of the particle contacts, we look at local quantities for each particle.

The particle instantaneous positions and velocities are shown in Fig. 6 for the TF-DEM simulation of the central-jet case. The

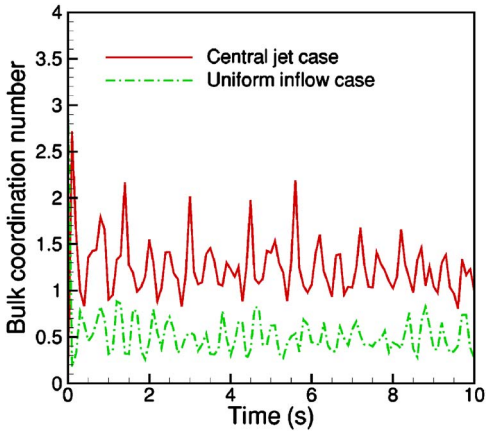

Fig. 5 The bulk coordination numbers as a function of time

particle movements and bed expansion behaviors are also in qualitative agreement with experimental observations. These agreements serve to initially substantiate the practicality of the hybrid TF-DEM model presented here. The number of contacting particles for each particle, N_c, is defined as the number of contacting neighbors of one particle. A direct interpretation of N_c is that a particle is in a binary collision when $N_c=1$, or is in a multicontact when $N_c>1$. The value of N_c for each particle is also presented in Fig. 6. From the results, it is clear that N_c is not distributed homogeneously in space. The value of N_c is low (1–2) in bubble regions but high in other regions (>2), which are mainly near the bottom corners of the bed after the jet penetrates the bed (see Figs. 6(*b*)–6(*d*)). High N_c shows that multicontacts prevail in those regions away from bubbles.

The spatial distributions of particle contact forces, drag forces, and ratios of these forces are shown in Fig. 7 for the central-jet case. The magnitudes of total forces in every computational cell are shown, i.e., the total contact force at a cell center, $\mathbf{f}_{cj}=\Sigma_i^{N_m}\mathbf{f}_{cji}$, and the total drag force at a cell center, $\mathbf{f}'_{gpj}=\Sigma_i^{N_m}\mathbf{f}'_{gpi}$, where i and j are indices of particles and grid nodes, respectively. The force is also scaled by the magnitude of the gravitational force of a particle. It can be seen from the instantaneous distributions (Fig. 7(*a*)) that the contact forces (left frame) are large in the

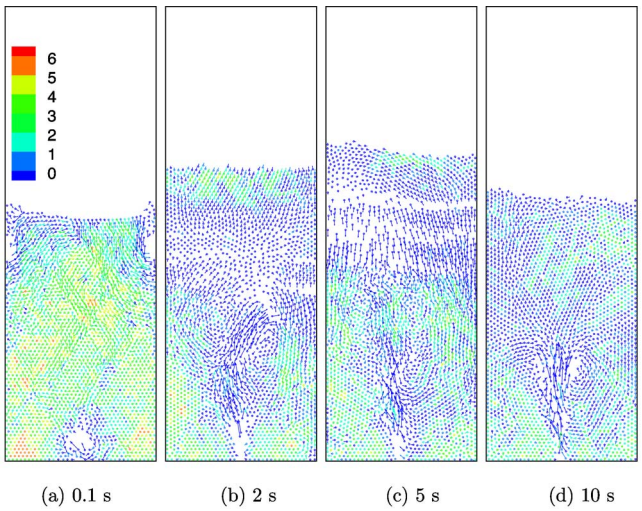

Fig. 6 Instantaneous particle positions and velocities for the central-jet fluidized bed, denoted by points and vectors. The contour levels show the magnitudes of N_c. The domain in the figure only shows 45 cm above the inlet.

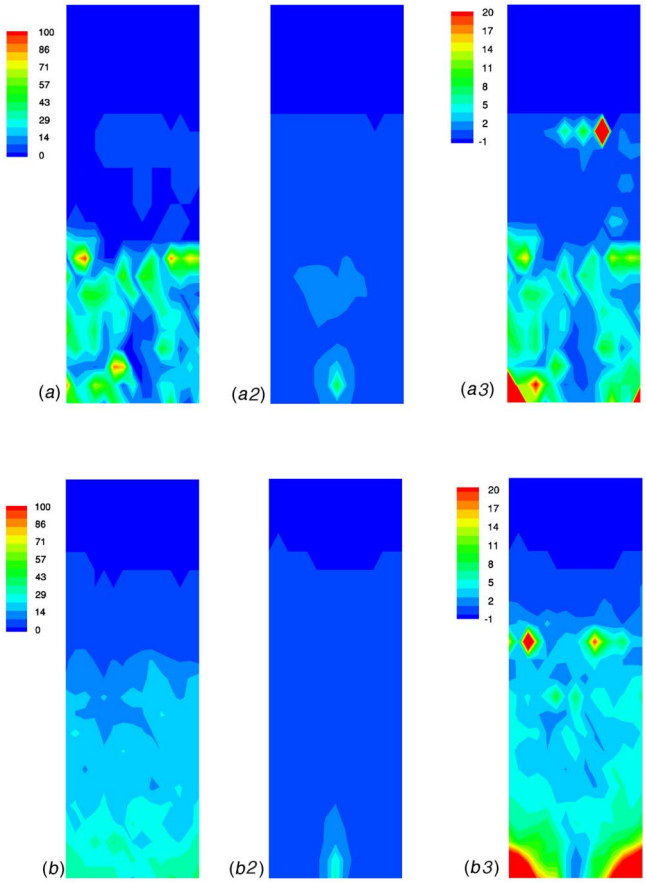

Fig. 7 Particle contact forces, drag forces, and their ratios for the central-jet fluidized bed for (*a*) the instantaneous distribution at 5 s and (*b*) the time-averaged distribution at 5–10 s. The left panels show contact forces, the middle panels show drag forces, and the right panels show the ratios of contact forces to drag forces. The left legends are the magnitudes of forces scaled by the gravitational force of a particle. The right legends are the ratios, where –1 indicates that the drag force is zero at that position. Note that the highest ratio of 100 is not shown in order to distinguish the majority of ratios below 20. The domain in the figure only shows 45 cm above the inlet.

regions away from bubbles, which is consistent with the experimental observation that higher particle pressure is generated under bubbles [5]. The instantaneous drag forces (shown in the middle frame of Fig. 7(*a*)) are large in the jet region. The ratios of contact forces to drag forces vary between 2 and 10 in most of the bed region. However, contact forces may be as high as 100 times that of the drag forces (higher than the maximum contour level shown in Fig. 7) in the corners beside the jet. The high contact force regions could also correspond to the high solid stress regions. The locations of large contact forces and force ratios are correlated with the locations of higher N_c, as compared to the corresponding snapshot at 5 s in Fig. 6. Solid volume fractions in most of these regions are less than the critical solid volume fraction ε_s^* (see the left panels in Fig. 8), and the solid stress is calculated using the KTGF. Since the solid stress calculated using the KTGF does not take into account the contribution from the collisions with $N_c>1$, the solid stresses in these regions are also expected to deviate from the stresses predicted using the KTGF. These observations emphasize the importance of studying particle contacts in the regions away from bubbles in order to understand the constitutive behavior of a fluidized bed. The time-averaged distributions (Fig. 7(*b*)) show similar trends although the forces are distributed more homogeneously.

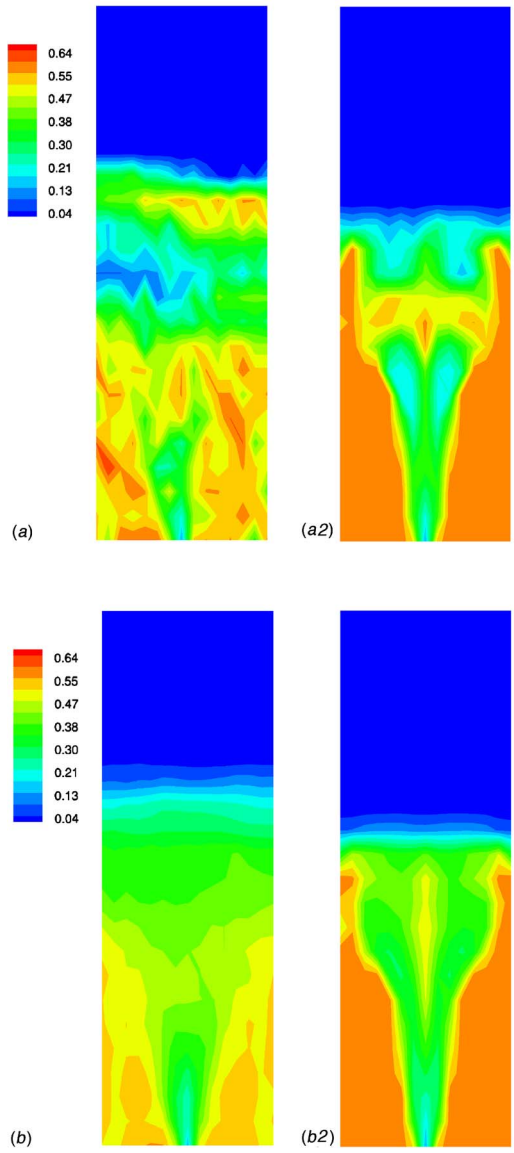

Fig. 8 Particle volume fractions for the central-jet fluidized bed for (*a*) the instantaneous distribution at 5 s and (*b*) the time-averaged distribution at 5–10 s. The left panel shows the TF-DEM simulation and the right panel shows the TFM simulation. The domain in the figure only shows 45 cm above the inlet.

A comparison between the solid volume fractions predicted by the TF-DEM model and those predicted by TFM is also performed. The instantaneous and time-averaged (5–10 s) solid volume fraction distributions for the central-jet case are shown in Figs. 8(*a*) and 8(*b*), respectively. The distributions demonstrate that the TF-DEM model and TFM model predict a similar jet penetration behavior. However, the TFM predicts a more homogeneous and symmetric distribution of solids. The TF-DEM model can capture the concentration difference in the corner regions, as seen in Fig. 8(*b*). The predicted differences reflect the inability of the TFM to capture the structural information although the TFM predicts a similar mean pressure drop as the TF-DEM model does. The inability may also be due to the solid constitutive closures used in the TFM. The closures do not adequately model the stress and energy dissipation caused by multicontacts, which reduces the preferential change in solid volume fractions. A quantitative account of the differences between the stresses and dissipation calculated using the TF-DEM and using the TFM is the subject of a future study [28].

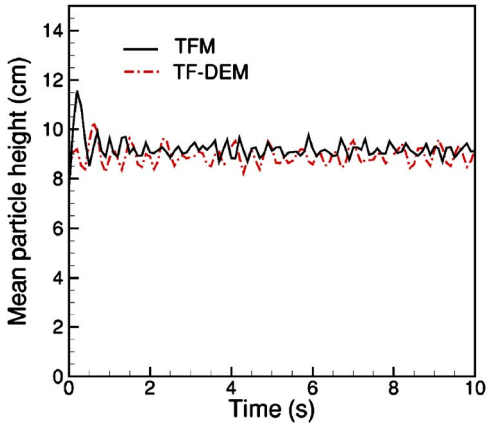

Fig. 9 The mean particle height as a function of time for the uniform inflow fluidized bed calculated from the TF-DEM model and TFM

For the uniform inflow case, bed dynamics were first analyzed by the time evolution of the mean particle height. The mean particle height is defined as the arithmetic mean of the heights of all particles in the bed. It is straightforward to calculate the particle height in the TF-DEM model, and it can also be estimated by a method defined in Ref. [26] for the TFM. The mean particle height as a function of time is shown in Fig. 9. It is found that mean particle heights predicted by both models fluctuate at a similar level. The 5–10 s time-averaged values are 8.9 cm and 9.16 cm for TF-DEM model and TFM, respectively. Both are lower than the experimental value of 11.4 cm [29]. The particles' instantaneous positions, velocities, and N_c are presented in Fig. 10. It can be seen that the bed is uniformly fluidized at the startup stage (Fig. 10(*a*)) with no bubble and zero N_c over almost the whole bed. After bubbles develop, higher N_c appear in regions away from the bubble; however, the ratio of the number of multicontacts over the total number of collisions is small, fluctuating around 0.3, as shown in Fig. 11. This small ratio indicates that the binary collision assumption in the KTGF may still be reasonable under this flow condition. In contrast, the ratio for the central-jet

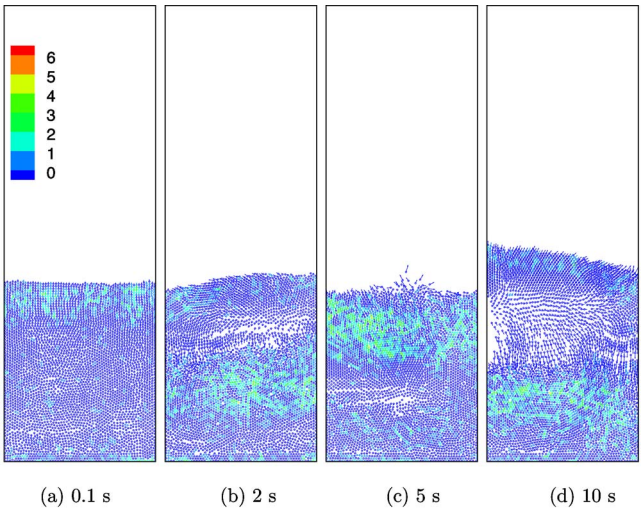

Fig. 10 Instantaneous particle positions and velocities for the uniform inflow fluidized bed denoted by points and vectors. The contour level shows the magnitude of N_c.

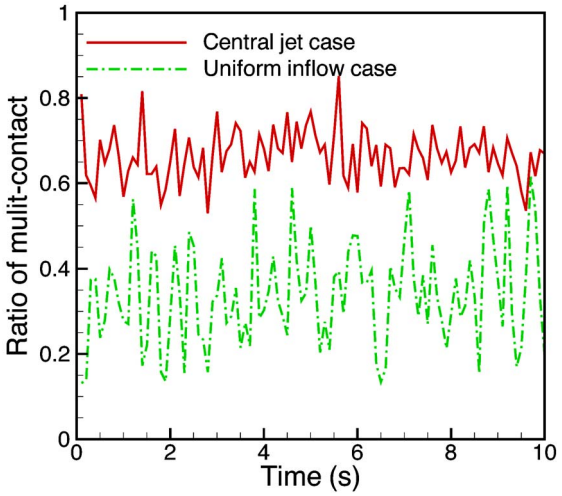

Fig. 11 The ratio of particles in multicontacts to the total number of particles in contact as a function of time

case is higher than 0.6 most of the time, which indicates that the binary collision assumption may deviate from the real particle collision scenario to a larger degree. The spatial distributions of particle contact forces, drag forces, and ratios of these forces for the uniform inflow case are also shown in Fig. 12. Similar observations can be drawn as for the central-jet case. However, there is no region where the contact forces are more than 15 times higher than the drag forces, as observed in the corner regions for the central-jet case.

The two different formulas for computing the effective drag force based on averaged or instantaneous particle velocities were applied to simulate the uniform inflow case. Since the method using the averaged particle velocities produces the same forces on each particle in a fluid cell, it tends to smear the difference between particle movement and results in less vigorous bed dynamics. It is expected that the method using instantaneous particle velocity will predict a higher bed expansion. This effect is actually shown by the time-averaged solid volume fraction in Fig. 13, where the result produced by the second method shows a slightly higher bed expansion. The time-averaged mean particle height predicted by the second method is 9.1 cm, and is higher than that

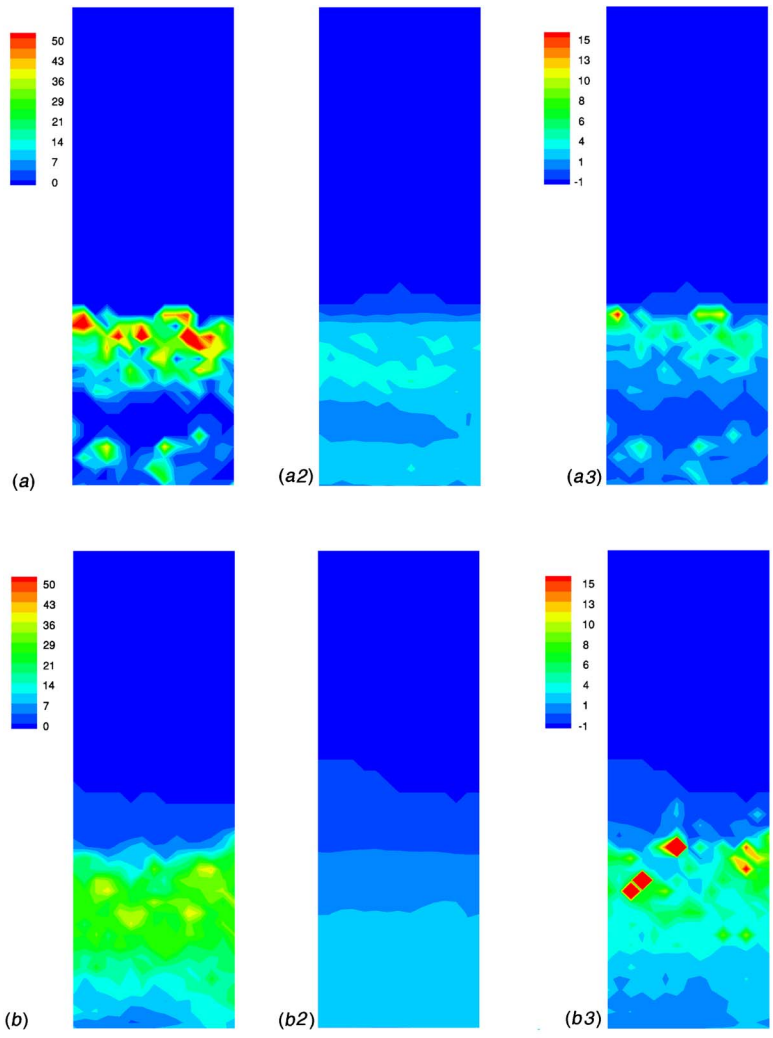

Fig. 12 Particle contact forces, drag forces, and their ratios for the uniform inflow fluidized bed for (*a*) the instantaneous distribution at 5 s and (*b*) the time-averaged distribution at 5–10 s. The left panels show contact forces, the middle panels show drag forces, and the right panels show the ratios of contact forces to drag forces. The left legends are the magnitudes of forces scaled by the gravitational force of a particle. The right legends are the ratios, where –1 indicates that the drag force is zero at that position.

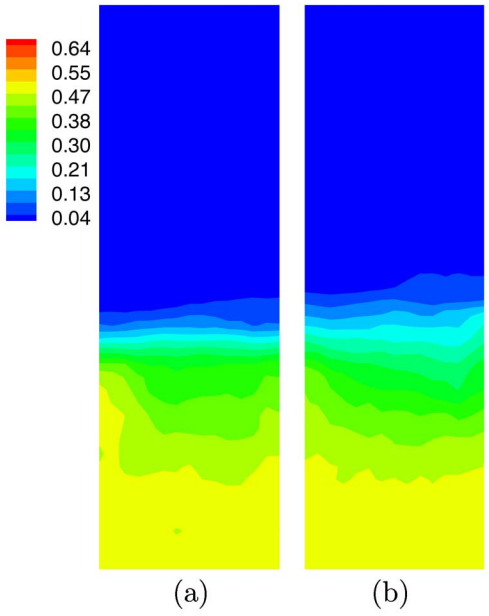

Fig. 13 Time average in the range of 5–10 s of the particle volume fractions for the uniform inflow fluidized bed predicted by the method using (*a*) averaged particle velocities and (*b*) instantaneous particle velocities

predicted by the first method. However, it should be noted that the difference between the mean quantities predicted by the two formulas is not large. Local quantities, such as granular temperature, will be further studied to investigate the effect of the formulas.

Conclusions

A methodology for a hybrid TF-DEM model for gas-solid fluidized beds has been presented. The model couples the DEM for particle dynamics with the TF equations for the gas phase. The coupling between the two phases is modeled by the gas-particle interaction force. Simulations of two types of gas-solid fluidized beds have been carried out using the hybrid simulation method. The results of the hybrid TF-DEM simulations are compared to experimental data and TFM simulations. It is found that the TF-DEM simulation is capable of predicting general fluidized bed dynamics, i.e., pressure drop across the bed and bed expansion, which are in agreement with experimental measurements and TFM predictions. The number of contacting particles N_c is found to be greater than 1 in the regions away from the bubble. The contact forces are much larger than the effective drag forces in the same regions. It is also demonstrated that multicontacts prevail in the central-jet fluidized bed, implying that the binary instantaneous collision assumption in the KTGF may not be applicable in this flow condition. For the uniform inflow fluidized bed, the number of contacting particles are around 1 to 2 so that the binary collision assumption is reasonable in this flow condition. With further research, the particle contact information will hopefully provide guidelines for a constitutive model development and may contribute to the subgrid modeling method proposed by Sundaresan [30]. The relations between the flow conditions and fluidized bed constitutive behaviors and how the multi-interactions should be incorporated into the constitutive modeling clearly need further investigation. It would be instructive to first compare the stresses computed using particle information from the TF-DEM simulations with the stresses computed using the KTGF or using the friction-kinetic model [31]. The stress analysis will be given in a following paper [28].

The effect of computing an effective drag force on a particle in terms of averaged or instantaneous particle velocities was demonstrated. It was shown that the formulation using instantaneous particle velocities better captures the force difference at the particle scale and predicts a higher bed expansion, which is closer to the corresponding experimental results. Furthermore, the statistical error in the estimation of the interphase momentum transfer term becomes high as the grid is refined. This motivates using more sophisticated kernel estimation methods to achieve optimal error control in both statistical error and discretization error [32,33].

Acknowledgment

The authors would like to thank Dr. Sreekanth Pannala and Dr. Dhanunjay Boyalakuntla at Oak Ridge National Laboratory and Dr. Madhava Syamlal at National Energy Technology Laboratory for their useful discussions and help on MFIX. In addition, the computer and technical support by the High Performance Computing Center at Iowa State University is appreciated. This work was supported by the National Energy Technology Laboratory (U.S. Department of Energy) under Contract No. DE-AC02-07CH11358.

Nomenclature

$\mathbf{C}$ = fluctuation in particle translational velocity (cm/s)
d = particle diameter (cm)
e = coefficient of normal restitution
$\mathbf{g}$ = acceleration of gravity (cm/s^2)
I = moment of inertia of a particle ($g\ cm^2$)
$\mathbf{I}$ = interphase momentum transfer (dyn/cm^3)
J_{coll} = rate of dissipation of translational fluctuation kinetic energy due to particle collisions ($g/cm\ s^3$)
J_{vis} = rate of dissipation of translational fluctuation kinetic energy due to interstitial gas viscous damping ($g/cm\ s^3$)
k = stiffness coefficient of a particle (dyn/cm)
m = mass of a particle (g)
$\mathbf{n}$ = unit normal vector from a boundary to particles
N = particle number
N_c = coordination number
N_g = total number of gas phase chemical species
N_{sm} = total number of solid phase (m) chemical species
P = pressure (dyn/cm^2)
$\mathbf{r}$ = position vector (cm)
R = rate of formation ($g/cm^3\ s$)
Re = Reynolds number
$\bar{\bar{S}}$ = stress tensor (dyn/cm^2)
t = time (s)
U = fluidization velocity (cm/s)
$\mathbf{u}$ = tangential displacement (cm)
$\mathbf{v}$ = velocity for gas and solids (cm/s)

Greek Letters

β = coefficient for drag forces ($g/cm^3\ s$)
δ = normal compression in particle collision (cm)
ε = volume fraction
γ = viscous damping coefficient (1/s)
Γ = rate of dissipation of rotational fluctuation kinetic energy ($g/cm\ s^3$)
Γ_{slip} = production of translational fluctuation kinetic energy due to gas-particle slip ($g/cm\ s^3$)
μ = coefficient of friction in DEM
μ_g = gas shear viscosity ($dyn\ s/cm^2$)
μ_{sm} = solid shear viscosity ($dyn\ s/cm^2$)
λ_g = gas second coefficient of viscosity ($dyn\ s/cm^2$)

λ_{sm} = solid second coefficient viscosity (dyn s/cm^2)
ω = angular velocity(1/s)
ρ = density (g/cm^3)
θ = translational granular temperature (cm^2/s^2)

Superscripts

p = plastic regime in granular flows
v = viscous regime in granular flows

Subscripts

cell = computational cell
coll = collision
g = gas phase
i = index of a particle
l = lth solid phase
m = mth solid phase
n = normal direction in the particle contact frame
t = tangential direction in the particle contact frame
M = number of phases
mf = minimum fluidization
max = maximum value
p = particle
s = solid phase
w = wall boundary

References

[1] Curtis, J. S., and van Wachem, B., 2004, "Modeling Particle-Laden Flows: A Research Outlook," AIChE J., **50**(11), pp. 2638–2645.

[2] Jackson, R., 2000, *The Dynamics of Fluidized Particles*, 1st ed., Cambridge University Press, Cambridge, UK.

[3] Gidaspow, D., Jung, J., and Singh, R. K., 2004, "Hydrodynamics of Fluidization Using Kinetic Theory: An Emerging Paradigm 2002 Flour-Daniel Lecture," Powder Technol., **148**, pp. 123–141.

[4] Agrawal, K., Loezos, P. N., Syamlal, M., and Sundaresan, S., 2001, "The Role of Meso-Scale Structures in Rapid Gas-Solid Flows," J. Fluid Mech., **445**, pp. 151–185.

[5] Rahman, K., and Campbell, C. S., 2002, "Particle Pressures Generated Around Bubbles in Gas-Fluidized Beds," J. Fluid Mech., **455**, pp. 102–127.

[6] Choi, J., Kudrolli, A., Rosales, R. R., and Bazant, M. Z., 2004, "Diffusion and Mixing in Gravity-Driven Dense Granular Flows," Phys. Rev. Lett., **92**(17), p. 174301.

[7] Bazant, M. Z., 2003, "A Theory of Cooperative Diffusion in Dense Granular Flows," Report No. cond-mat/0307379.

[8] Bazant, M. Z., 2006, "The Spot Model for Random-Packing Dynamics," Mech. Mater., **38**(8–10), pp. 717–731.

[9] Tsuji, Y., Kawaguchi, T., and Tanaka, T., 1993, "Discrete Particle Simulation of Two-Dimensional Fluidized Bed," Powder Technol., **77**, pp. 79–87.

[10] Hoomans, B. P., Kuipers, J. A., Briels, W. J., and van Swaaij, W. P., 1996, "Discrete Particle Simulation of Bubble and Slug Formation in a Two-Dimensional Gas-Fluidised Bed: A Hard-Sphere Approach," Chem. Eng. Sci., **51**(1), pp. 99–118.

[11] Xu, B. H., and Yu, A. B., 1997, "Numerical Simulation of the Gas-Solid Flow in a Fluidized Bed by Combining Discrete Particle Method With Computational Fluid Dynamics," Chem. Eng. Sci., **52**(16), pp. 2785–2809.

[12] Kafui, K. D., Thornton, C., and Adams, M. J., 2002, "Discrete Particle-Continuum Fluid Modelling of Gas-Solid Fluidised Beds," Chem. Eng. Sci., **57**, pp. 2395–2410.

[13] Syamlal, M., Rogers, W., and O'Brien, T., 1993, "MFIX Documentation: Theory Guide," National Energy Technology Laboratory, Department of Energy, Technical Note Nos. DOE/METC-95/1013 and NTIS/DE95000031 (see also http://www.mfix.org).

[14] Syamlal, M., 1987. "The Particle-Particle Drag Term in a Multiparticle Model of Fluidization," National Energy Technology Laboratory, Department of Energy, Topical Report Nos. DOE/MC/21353-2373, and NTIS/DE87006500.

[15] Syamlal, M., 1987, "A Review of Granular Stress Constitutive Relations," National Energy Technology Laboratory, Department of Energy, Technical Note Nos. DOE/MC21353-2372 and NTIS/DE87006499.

[16] Jenike, A. W., 1987, "A Theory of Flow of Particulate Solids in Converging and Diverging Channels Based on a Conical Yield Function," Powder Technol., **50**, pp. 229–236.

[17] Schaeffer, D. G., 1987, "Instability in the Evolution Equations Describing Incompressible Granular Flow," J. Differ. Equations, **66**, pp. 19–50.

[18] Cundall, P. A., and Strack, D. L., 1979, "A Discrete Numerical Model for Granular Assemblies," Geotechnique, **29**, pp. 47–65.

[19] Silbert, L. E., Ertas, D., Grest, G. S., Halsey, T. C., Levine, D., and Plimpton, S. J., 2001, "Granular Flow Down an Inclined Plane: Bagnold Scaling and Rheology," Phys. Rev. E, **64**(5), p. 051302.

[20] Boyalakuntla, D., 2003, "Simulation of Granular and Gas-Solid Flows Using Discrete Element Method," Ph.D. thesis, Carnegie Mellon University, Pittsburgh, Pennsylvania.

[21] Anderson, T. B., and Jackson, R., 1967, "A Fluid Mechanical Description of Fluidised Beds," Ind. Eng. Chem. Fundam., **6**, pp. 527–539.

[22] Ergun, S., 1952, "Fluid Flow Through Packed Columns," Chem. Eng. Prog., **48**, pp. 89–94.

[23] Wen, C. Y., and Yu, Y. H., 1966, "Mechanics of Fluidization," *Fluid Particle Technology*, Chemical Engineering Progress Symposium Series Vol. 62, American Institute of Chemical Engineers, New York, pp. 100–111.

[24] Syamlal, M., 1998, "MFIX Documentation: Numerical Technique," National Energy Technology Laboratory, Department of Energy, Technical Note Nos. DOE/MC31346-5824 and NTIS/DE98002029 (see also http://www.mfix.org).

[25] Goldschmidt, M. J., Link, J. M., Mellema, S., and Kuipers, J. A., 2003, "Digital Image Analysis Measurements of Bed Expansion and Segregation Dynamics in Dense Gas-Fluidised Beds," Powder Technol., **138**, pp. 135–159.

[26] Sun, J., and Battaglia, F., 2006, "Hydrodynamic Modeling of Particle Rotation for Segregation in Bubbling Gas-Fluidized Beds," Chem. Eng. Sci., **61**(5), pp. 1470–1479.

[27] Sun, J., Battaglia, F., and Subramaniam, S., 2006, "Dynamics and Structures of Segregation in a Dense, Vibrating Granular Bed," Phys. Rev. E, **74**(6), p. 061307.

[28] Sun, J., and Battaglia, F., 2007, "Analysis of Solid Structures and Stresses in a Gas Fluidized Bed," American Society of Mechanical Engineers, Fluids Engineering Division (Publication), FED Report No. FEDSM2007-37189.

[29] Goldschmidt, M., 2001, "Hydrodynamic Modelling of Fluidised Bed Spray Granulation," Ph.D. thesis, Twente University, Netherlands.

[30] Sundaresan, S., 2000, "Modeling the Hydrodynamics of Multiphase Flow Reactors: Current Status and Challenges," AIChE J., **46**(6), pp. 1102–1105.

[31] Srivastava, A., and Sundaresan, S., 2003, "Analysis of a Frictional-Kinetic Model for Gas-Particle Flow," Powder Technol., **129**, pp. 72–85.

[32] Dreeben, T. D., and Pope, S. B., 1992, "Nonparametric Estimation of Mean Fields With Application to Particle Methods for Turbulent Flows," Sibley School of Mechanical and Aerospace Engineering, Cornell University, Technical Report No. FDA 92-13.

[33] Garg, R., Narayanan, C., Lakehal, D., and Subramaniam, S., 2007, "Accurate Numerical Estimation of Interphase Momentum Transfer in Lagrangian-Eulerian Simulations of Dispersed Two-Phase Flows," Int. J. Multiphase Flow, doi: 10.1016/j.ijmultiphaseflow.2007.06.002